RSC Advances

PAPER

View Article Online
View Journal | View Issue

Cite this: *RSC Adv.*, 2022, **12**, 27321

Inter-coffee-ring effects boost rapid and highly reliable SERS detection of TPhT on a light-confining structure

Dai Yujie,[ad] Jiang Shuai,[b] Gao Yangyang,[ac] Pan Hongyue,[c] Liu Ke[c] and Chang Lin *[ad]

Triphenyltin chloride (TPhT) is a widely applied toxic compound that poses a significant threat to humans and the environment. Surface-enhanced Raman spectroscopy (SERS), capable of non-destructive, rapid, and trace detection, is desirable to better evaluate its distribution and content. However, a sensitive method with simple measuring protocols which maintains excellent reproducibility remains challenging. Here, we proposed an inter-coffee-ring effect to accelerate the sampling and measuring process while maintaining highly reproducible results. Two overlapping coffee-rings are formed through sequenced drying of gold nanorod colloids and a gold nanorod TPhT mixture on a superhydrophobic light-confining structure. Both the gold nanorods and the TPhT are enriched in the overlapping region. The gold nanorods reordered in such an area under the inter-coffee-ring effect yielded vast numbers of consistent hotspots at the sub-2 nm level. Such consistency leads to excellent SERS performance under the light-confining effect induced by the nanoarray substrates. The detection limits of the probe molecule R6G reached 10^{-12} M, and TPhT reached 10^{-8} M while achieving excellent stability and reproducibility, and a linear regression coefficient above 0.99 was achieved for TPhT. Crucially, the visible nature of the inter-coffee-ring overlap enabled rapid measurements, thus providing robust support for detecting environmental pollutants.

Received 20th July 2022
Accepted 12th September 2022

DOI: 10.1039/d2ra04494c

rsc.li/rsc-advances

Introduction

As a class of environmental endocrine disruptors, organotin compounds can cause harm to the environment and the human reproductive system.[1] Among them, triphenyltin chloride (TPhT) is widely used in pesticides and paints and poses a significant threat to the water environment and human health.[2] Therefore, it is crucial to establish a rapid, non-destructive, and sensitive method for its detection and monitoring. As an analytical technique, surface-enhanced Raman spectroscopy (SERS) is a fingerprint scattering spectroscopy that enables rapid and non-destructive detection of molecules.[3–6] It has been widely used in the field of environmental monitoring and is particularly suitable for the on-site detection of environmental pollutants as the detection limits can reach as low as the single-molecule level, depending on the performance of the substrate, and less pretreatment of the sample is needed.[7–10]

Although SERS technology has been developed for decades, there are still specific problems and challenges in practical applications.[11–14] The preparation of SERS substrates with high sensitivity while obtaining robust reproducibility and stability is the main problem with SERS technology.[15–18] The present state of the art SERS substrates mainly include chip-based[19–21] and colloidal substrates,[22–26] and series substrates have been fabricated to detect TPhT. Among them, Shan Jiang *et al.*[27] fabricated a honeycomb-like arrayed substrate, and the LOD of the TPhT detection reached 10^{-10} M with a relatively good linear regression coefficient of 0.97. However, locating the measuring point when the sample is fully evaporated is challenging, for the droplet dry mark at trace concentration is invisible to the naked eye. Researchers often need plenty of tests during measurements to acquire the representative spectra. This induced a time-consuming measuring process, which is unwanted in the application, resulting in a linear regression coefficient below 0.99. Moreover, such drawbacks are common in all chip-based substrates. Juan Jiang *et al.*[28] dispersed silver nanoparticles on a TPhT-soaked apple and obtained a semi-quantitative detection of TPhT and a 0.6 ng L^{-1} detection limit. However, the random distribution of the nanoparticles on the apple peel precluded accurate quantification. It is still worth mentioning that the dry nanoparticle mark on the apple peel has made such a method convenient for non-professionals. Such convenience is significant for the practical application of SERS substrates. Therefore, colloidal nanoparticles mixed with analytes are a potential pathway to conduct a rapid test that can easily find the sample point. Compared with the chip-based substrates'

[a]*Chongqing Institute of Green and Intelligent Technology, Chinese Academy of Sciences, Chongqing, China, 400714. E-mail: 294301050@qq.com*
[b]*China CEC Engineering Corporation, Chang Sha, China, 410114*
[c]*China Three Gorges Construction Engineering Corporation, Chengdu, China, 610041*
[d]*University of Chinese Academy of Sciences, Beijing, China, 100049*

high consistency and stability, colloidal substrates feature high sensitivity owing to the strong coupling of plasmonic nanoparticles. The aggregation of nanoparticles forms vast numbers of hotspots, enabling ultrasensitive detection. However, the reproducibility and stability of colloidal substrates are low due to random aggregation and heterogeneous distribution under the coffee-ring effect. Specifically, when acquiring Raman spectra on a specimen from a dried droplet of the plasmonic nanoparticle and analyte mixture, it is often challenging to locate the sampling point while keeping high reproducibility. That is mainly attributed to the uneven distribution of the analytes, plasmonic particles, and variable absorption.

Our aim was to achieve a rapid detection protocol while obtaining high sensitivity, reproducibility, and stability. We combined chip-based substrates with plasmonic gold nanorods to create an inter-coffee-ring mark that is easy to locate using the naked eye through an analysis of the advantages and disadvantages of two types of substrates. The inter mark is created by sequencing dropwise and drying the plasmonic nanoparticle solution and the plasmonic nanoparticles/analytes mixture. Such a procedure is especially beneficial for a fast-sampling measurement. Moreover, the plasmonic gold nanorods and the analytes possess the highest concentration on this overlapping mark. It is easy to locate the laser spot on such a mark to obtain ultrasensitive detection. Besides, the chip-based substrates are manufactured with nanoarray patterns to enhance the intensity of gold nanorods LSPR by using the light-confining effect. A superhydrophobic modification is conducted to achieve better enrichment during sample evaporation. All of which contribute to a better performance of the substrates. By coupling the advantages of the two types of substrates, we achieved a significant increase in sensitivity with high reproducibility and stability, providing strong support for the rapid and quantitative detection of TPhT.

Results and discussion

Inter-coffee-ring effect

SERS technology has long been used as a rapid protocol with high sensitivity, reproducibility, and stability. For chip-based SERS measurements, the sample at trace concentration is always invisible under optical microscopy. Although it could be avoided in liquid state measurements, the requirements for the substrates of a higher signal enhancement are difficult to achieve. The dry mark is easy to locate for colloidal substrates under optical microscopy, yet a lack of reproducibility hindered its application. Its sensitivity will be weakened when measuring the colloidal mixture in a liquid state. Therefore, neither the chip-based nor the colloidal-based substrates can achieve an excellent application performance.

Herein, we proposed an inter-coffee-ring strategy for a rapid sampling procedure while maintaining sensitivity and reproducibility on the coffee-ring. The coffee-ring effect is always considered a shortcoming of sampling methods that use colloidal substrates. However, the enrichment of analytes and colloids on the coffee-ring helps promote the substrate's sensitivity. Only the random agglomeration of plasmonic nanoparticles led to variable hotspots and irreproducible results.

The inter-coffee-ring effect is based on a phenomenon occasionally observed during our experiments. When drying the colloidal solution on a wafer, most nanoparticles migrated to the coffee-ring with a random arrangement, as can be expected by all researchers in this discipline. However, when another droplet dried, overlapping with the first mark, a re-assembling process occurs in the inter-ring region, denoting the phenomenon as the inter-coffee-ring effect. The specific procedure and assembling result are shown in Fig. 1. Fig. 1a is the sampling procedure that introduces the inter-coffee-ring effect. Two droplets were sequentially dried on the substrates and before the second droplet, the first dried coffee-ring mark was rinsed with deionized water. Otherwise, the excess surfactant in the coffee-ring will drag the second drop to fuse with the first ring. Fig. 1b shows the potential mechanism of the re-assembling process. When drying the first droplet on the substrates, a random distribution of gold nanorods is formed on the ring mark, depicted as a yellow ring. After applying the second drop to the overlapping region (a bluish color), the pre-aggregated gold nanorods and the gold nanorods in the second drop will migrate under capillary force. Specifically, part of the pre-aggregated gold nanorods desorbs from the surface, especially the weak absorbed and low alignment ones. Together, the gold nanorods in the second drop migrate and assemble on the interlapping region until an enhanced alignment formation. The re-assembling results are shown in Fig. 1c–f. As depicted, the gold nanorods on the non-overlapping region are distributed without alignment and the orderliness of the gold nanorod in the overlapping area is significantly enhanced. The inter-coffee-ring effect is a simple sampling method that requires non-professional skills for application and thus is suitable for on-site and rapid detection of pollutants in the environment.

Inter-coffee-ring performance

To ascertain the performance of the inter-coffee-ring method, a superhydrophobic light-confining structure integrated with a pre-aggregated gold nanorod coffee-ring was fabricated as a demonstration. The light-confining structure in this demonstration was customized to protect the gold nanorod from desorption and enhance its stability. When using a flat substrate as the back plate, the gold nanorod on the first ring mark can be easily destroyed, leading to weak mechanical properties and irreproducible results. The light-confining structure is constructed with a nanopillar array pattern composed of a periodical concave and convex structure, where the gold nanorod aggregates into the concaves. The substrate is also coupled with superhydrophobic modification to prevent the gold nanorod from desorption. Such a modification could help avoid the nano aggregates from contacting the following droplet or rinse, for the superhydrophobic hierarchical structure tends to interact with water in a Cassie–Baxter state. Together with the structure's spatial resistance, the gold nanorods are stuck in the concaves.

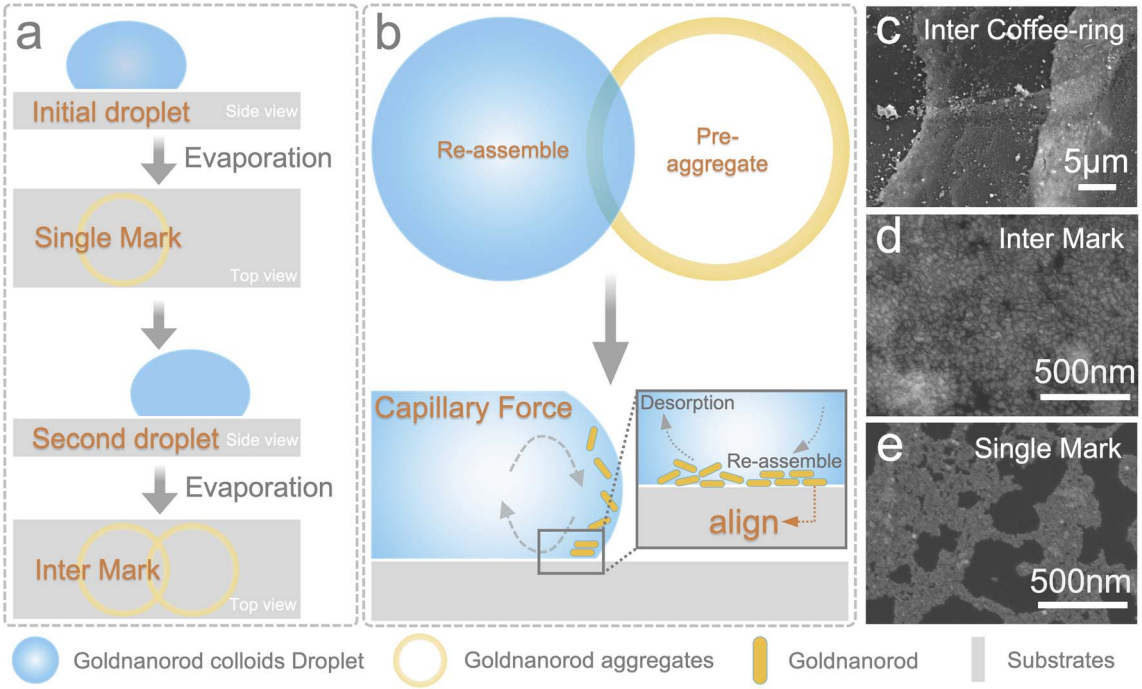

Fig. 1 GNRs re-assembling driven by a double coffee-ring effect: (a) the inter-coffee-ring formation on the silicon wafer, (b) the magnified gold nanorods re-assembling region and potential assembling mechanism, (c) gold nanorods' distribution on the inter-coffee-ring mark, (d) gold nanorods' alignment on the inter-coffee-ring region, (e) gold nanorods' distribution on the single coffee-ring mark.

Fig. 2a presents the morphology of the light-confining structures characterized by FESEM. The structure unit is measured to be 1 μm high, and the diameter on top and bottom is 500 nm and 800 nm, respectively. The top-view image demonstrated that a light-confining array with a near-circular structure had a highly ordered arrangement with a structural period of about 2 μm. The mask for this structure is circular, yet the prepared structure is not a standard circular shape. Also, wrinkles could be observed on the pillar array, as shown in Fig. 2b. Such a morphology is the result of wet etching. In wet etching, layer-by-layer exfoliation of Si atoms occurs on the 100-crystal-oriented silicon wafer. The steepness of dry etching

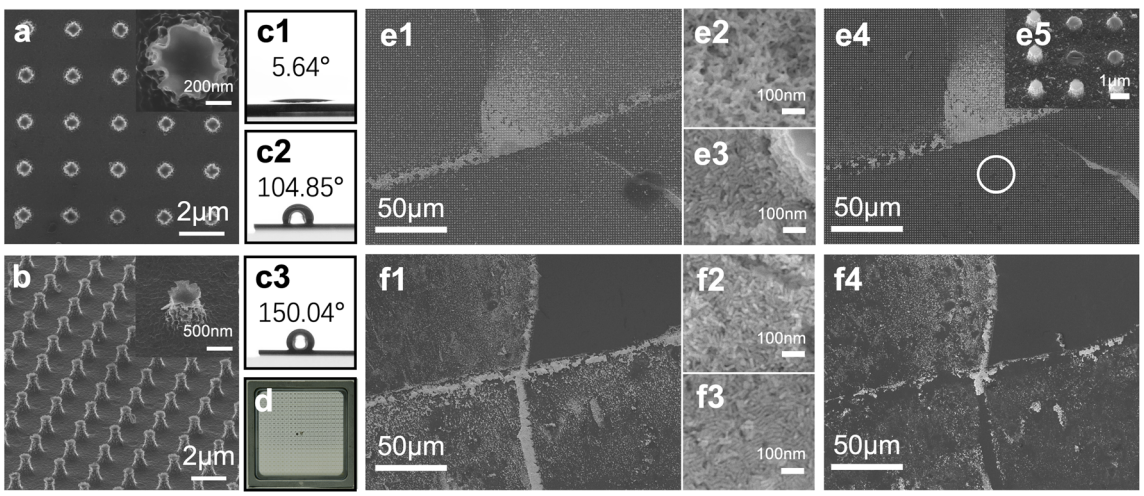

Fig. 2 (a) Top and (b) side view SEM images of the light-confining structures. The contact angle of (c1) untreated silicon wafer, (c2) untreated light-confining structures, and (c3) superhydrophobic light-confining structures. (d) The rapid localizing stage for the inter-coffee-ring mark comparison before and after ultrasonication. (e1) The inter-coffee-ring mark on the light-confining structures, the inset is the inter-coffee-ring mark after ultrasonication. (e2) Single coffee-ring aggregates on the light-confining structure. (e3) Inter-coffee-ring assembly on the light-confining structure. (e4) The ultrasonicated inter-coffee-ring mark on light-confining structures. (e5) Structure breakdown after ultrasonication. (f1) The inter-coffee-ring mark on a silicon wafer, the inset is the inter-coffee-ring mark after ultrasonication. (f2) Single coffee-ring aggregates on a wafer. (f3) Inter-coffee-ring assembly on a wafer. (f4) Ultrasonicated inter-coffee-ring mark on a wafer.

cannot be achieved because the Si crystal has a face-centered cubic structure. Thus, its exfoliation direction agrees with the lattice and results in a rough surface. However, the roughness can further enhance the near-field enhancement. Although the present structure is not a smooth columnar structure at the nanoscale, the inter-structure still has excellent uniformity. Crucially, the wet etching method is easy to implement and low cost and is thus applicable for environmental monitoring applications.

The surface roughness induced a micro–nano hierarchical structure, essential for hydrophobic surfaces and enhancing their hydrophobicity. The more hydrophobic the structure surface is, the larger the concentrate coefficient of the droplet, and the less amount of the sample is needed. Therefore, we modified perfluorinated alkyl groups on the substrate with FDTS to enhance their hydrophobicity. As FDTS contains a trichlorosilane group at one end, it reacts with the hydroxyl group. It dehydrates hydrogen chloride to form siloxane under high-temperature conditions, and the perfluorinated group at the other end is then chemically bonded to the surface. The modification performance is illustrated in Fig. 2c1–c3. Fig. 2c1 shows the WCA (water contact angle) of an untreated silicon wafer, Fig. 2c2 shows the WCA of untreated light-confining structures, and Fig. 2c3 shows the superhydrophobic performance of the FDTS modified light-confining structures. As noted, the hydrophobicity of the FDTS-modified light-confining structure is greatly enhanced, and the WCA reaches 150.04°. Meanwhile, the WCA of the light-confining structure without modification is 104.85°, and the WCA of silicon wafer without modification is only 5.64°, which is not conducive to the enrichment of pollutants.

After the fabrication and modification of light-confining structures, two droplets of gold nanorod colloids were sequentially applied and evaporated on the structures. The assembling performance in the structure is evaluated and demonstrated in Fig. 2e. Fig. 2e1 is the inter-coffee-ring mark on the substrates. The marker range is approximately 884 μm^2, and the shape resembles an equilateral triangle with 50 μm sides, sufficient for multiple measurements. Fig. 2e2 and e3 are the morphology of gold nanorods on the single coffee-ring and inter-coffee-ring marks. The alignment of the gold nanorods on the inter-coffee-ring mark is significantly enhanced compared to the random distribution on the single coffee-ring mark. Fig. 2f1 shows the inter-coffee-ring mark on a wafer. The gold nanorod distributions are also shown in Fig. 2f2 as the single coffee-ring aggregation and Fig. 2f3 as the inter-coffee-ring assembly. The alignment of gold nanorods on a wafer and the light-confining structure demonstrates the inter-coffee-ring effect. The orderliness of the overlapping region is much higher than that of the single ring mark. Such alignment is significant for better reproducibility. The assembling of gold nanorods on the wafer and the substrate also proves the non-specific nature of the inter-coffee-ring effect. Thus, the nanoparticle morphology and the substrate structure can be tailored for specific applications.

Further, the stability of the structure was evaluated through a 30 min ultrasonication. The distribution and immobilization performance are compared *in situ* using a customized FESEM rapid localizing sample stage. Fig. 2d is the ruler of the rapid localizing sample stage. The inter-coffee-ring mark is easy to locate after the ultrasonication by the ruler. The treated morphologies are shown in Fig. 2e4 and e5. Compared to the mark before ultrasonication, the peel-off effect on the wafer is more severe, yet the morphology changes of the light-confining structure can barely be seen. Additional, numerous black dots marked by a white circle in Fig. 2e4 are the mechanical breakdown of the light-confining structure, as shown in Fig. 2e5, a testament to the intense cleansing of the ultrasonication. The mechanical breakdown of the light-confining structure further proved the robust stability of the substrates. The orderly assembled gold nanorods are stably trapped in the light-

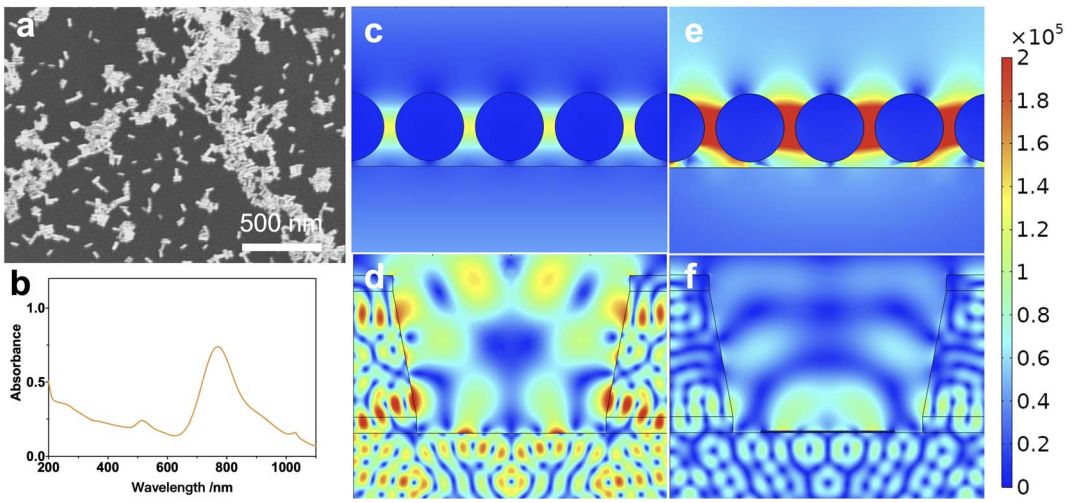

Fig. 3 (a) Morphology of the gold nanorods, (b) UV-visible spectrum of the gold nanorods. (c) Simulation of the gold nanorods electric field distribution on the surface of a silicon wafer, (d) simulation of light-confining structures' electric field distribution, (e) simulation of the electric field distribution of gold nanorods on the surface of light-confining structures, and (f) simulation of electric field distribution of light-confining structures with gold nanorods distributed on the surface.

confining structure, other than peeling off from the wafer's flat surface. Such stability is essential for an excellent SERS substrate.

The specific SERS performance of the substrates is characterized further to clarify the superiority of the inter-coffee-ring effect coupling. The morphology of the gold nanorods is shown in Fig. 3a. The length and diameter of nearly 100 gold nanorods are measured using ImageJ to calculate the specific dimensions of the gold nanorods. The mean diameter and length are 12 nm and 43 nm. The average gap size between the gold nanorods was 2 nm, corresponding to the kinetic radius of surface adsorbed CTAB on the gold nanorods. Fig. 3b shows the UV-vis spectrum of the gold nanorod colloids. The LSPR peak was found to be 781 nm, coupled superbly with the 785 nm diode laser source, so the 785 nm light source was used as the excitation source in the subsequent tests.

The synthesized gold nanorods are calculated to be 1 nM. In the probe molecule detection, the gold nanorods colloids are washed with deionized water twice, dispersed in 5 mM CTAB, and concentrated to 5 nM. The mix ratio of the probe molecule to gold nanorods colloids is one. 10 μL gold nanorods colloids and the mixture are sequentially dropped and dried on the light-confining structure. The gold nanorods migrated and assembled on the inter-coffee-ring region under the capillary force. Under the coupling effects of coffee-ring and hydrophobicity, both the gold nanorods and the analytes enriched the coffee-ring, improving the substrate's sensitivity. After the drop is wholly volatilized, a hybrid self-assembly system is formed inside the light-confining structure. Moreover, the analytes are adequately adsorbed on the gold nanorods' surface in the evaporation process and distributed in the hotspot region sufficiently. The morphology of the light-confining structure also induced a trap-in of the colloids, locating all the mixture in the light-confining area, thus enhancing the electric field intensity.

Numerical simulations were conducted using a 785 nm plane-wave light source to evaluate the coupling performance of gold nanorods and light-confining structures. The corresponding results are shown in Fig. 3c–f, including the electric field distribution of light-confining structures, gold nanorods on the silicon wafer, and gold nanorods in the light-confining structure. The maximum electric field intensity of the gold nanorods on a wafer is 1.4×10^5 V m^{-1}, as shown in Fig. 3c. The peak electric field intensity of the gold nanorods in the light-confining structures is 5.5×10^5 V m^{-1}, as shown in Fig. 3e. The coupling of gold nanorods and the light-confining structure caused a substantial enhancement of the field intensity and a reduction of the electric field around the gold nanorods (Fig. 3f) compared to the light-confining structure (Fig. 3d). This is mainly due to the localization of the electric field on the gold nanorods, *i.e.*, the localized surface plasmon resonance (LSPR effect), the physical basis of the SERS effect. In conclusion, after distributing the gold nanorods in the light-confining structures, the intensity of the electric field distribution around them is enhanced by a factor of about four, which validates the coupling enhancement effect of the light-confining structures with the noble metal nanoparticles.

The Raman performance of the substrates was characterized using *p*-ATP and R6G as probe molecules, respectively. Among them, *p*-ATP contains the sulfhydryl group, which can bond adequately to the gold surface and is used to compare the sensitivity of different structures. R6G is a commonly used standard probe molecule for substrate performance evaluation. The substrate's performance, including the limit of detection, reproducibility, and stability, was assessed using different concentrations of R6G.

Fig. 4a shows the distribution of the two coffee-ring on the substrates, which were acquired using AZTEC large area mapping technology. Enrichment of the gold nanorods and the analytes on the coffee-ring is confirmed through the EDS spectra, as shown in Fig. 4b and c. Fig. 4d illustrates the comparison of the substrate performance, including light-confining structures, gold nanorods, and light-confining structures coupled with gold nanorods. The light-confining structures show a minor enhancement with a corresponding average signal intensity of 373.4 cps at 1078 cm^{-1}. The intensity on the gold nanorods is significantly enhanced, with a mean value of 24 482.8 cps. When using the gold nanorods coupled with light-confining structures, the signal intensity is substantially improved with a mean intensity of 109 805.6 cps, which was 294.07-fold the signal intensity of the light-confining substrate and 4.48-fold higher than the gold nanorods. Thus, the significance of the light-confining effect and the coupling effect of the gold nanorods and the light-confining structure was demonstrated.

The sensitivity of the substrates was further characterized and a limit of detection for R6G down to 10^{-12} M was achieved using the gold nanorods-coupled light-confining structure substrate. The result is shown in Fig. 4e. The average enhancement factor (AEF) is usually used to assess the sensitivity of a SERS substrate, and the following eqn (1) was applied for its calculation.

$$\mathrm{AEF} = \frac{I_{\mathrm{SERS}}}{I_{\mathrm{Raman}}} \Big/ \frac{N_{\mathrm{SERS}}}{N_{\mathrm{Raman}}} \tag{1}$$

where I_{SERS} represents the signal intensity of the SERS measurements, and N_{SERS} stands for the number of molecules. I_{Raman} and N_{Raman} correspond to the value of normal Raman acquisition.

The AEF of the substrate was calculated based on *p*-ATP as the occupancy of a single *p*-ATP is predicted to be 4 nm^2 according to Chemspider. The excitation volume in the laser spot is 1 μm in radius and 25 μm in depth. Before measurement, the ATP was allowed to fully absorb on the gold nanorods and rinsed after coffee-ring formation to exclude the concentrate effect. The peak intensity at 1078 cm^{-1} on the wafer is 382.5, and the intensity on the substrate is 109 805.9. Thus, the AEF is calculated to be 2.08×10^6.

Apart from sensitivity, reproducibility and stability are also characterized. To validate its reproducibility performance, the signal intensity of R6G absorbed on the substrates within the inter-coffee-ring mark and single coffee-ring mark are acquired. The data for reproducibility are collected from 20 randomly picked points. The variability between different R6G spectral

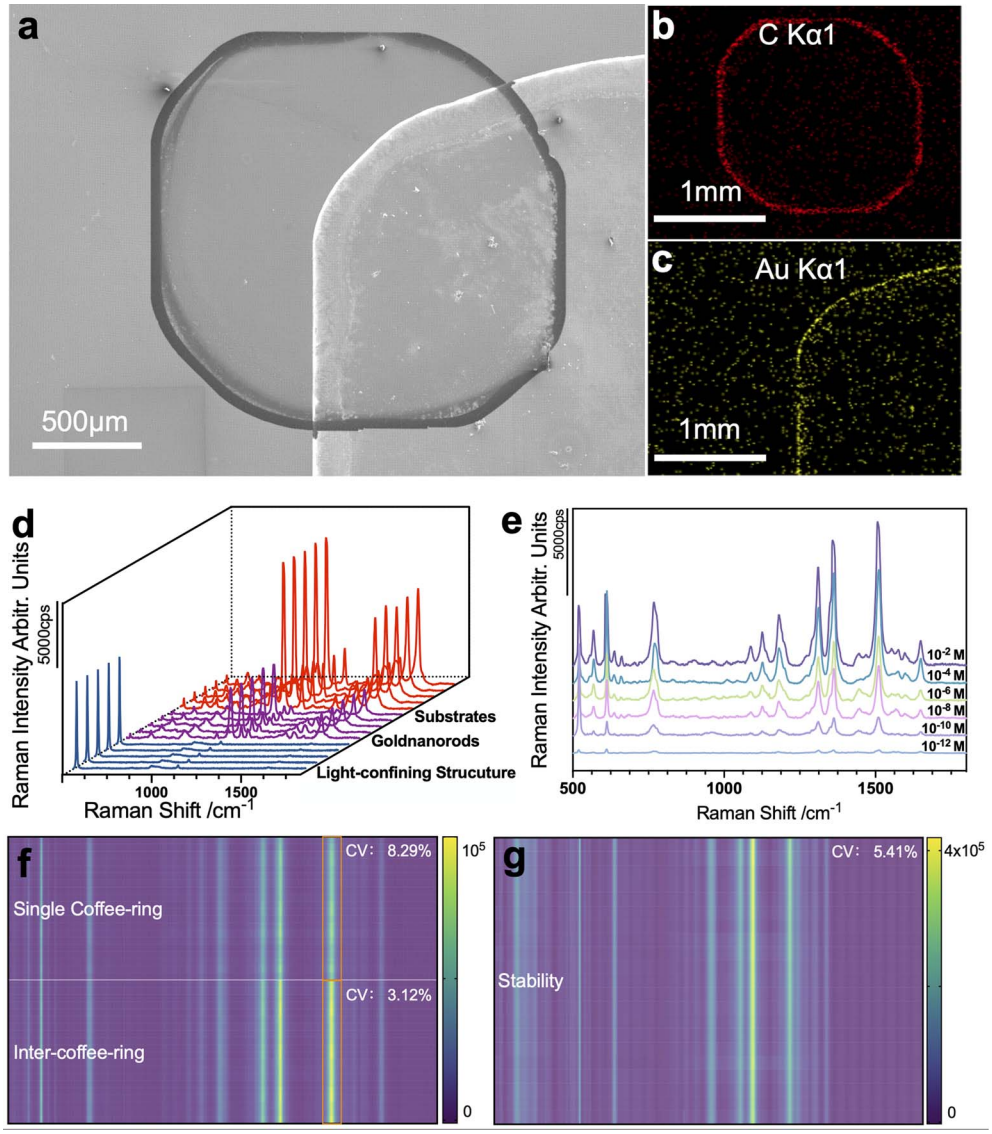

Fig. 4 (a) The inter-coffee-ring mark on light-confining structures, (b) the distribution of R6G on the second coffee-ring, (c) the distribution of GNRs on the first coffee-ring, and (d) *p*-ATP Raman spectra adsorbed by gold nanorods, 5 randomly picked points in the inter-coffee-ring region on a light-confining structure, gold nanorods applied on a wafer, and gold nanorods assembled on a light-confining structure. (e) Signal intensity of R6G in various concentrations mixed with gold nanorods and applied to the light-confining structure. (f) Reproducibility of spectra acquired on the inter-coffee-ring and single coffee-ring on the light-confining structure. (g) Stability of the inter-coffee-ring method.

peaks was calculated, with a coefficient of variation of only 3.12%. The substrates exhibited excellent reproducibility, especially compared to the 8.29% variation of single coffee-ring measurements.

An ultrasonication process characterized the stability of the coupling substrates. Further, to prove its stability in spectra intensities, the spectra of R6G on a single spot were acquired multiple times. Fig. 4g shows the spectra intensity acquired through continuous exposure. The results exhibit a stable characteristic peak intensity with a coefficient of variation of 5.41%.

SERS application of TPhT

Eventually, to obtain the actual detection performance of the substrate, TPhT was selected as the analyte, and different concentrations of TPhT were spiked in tap water. All spectra were acquired in the inter-coffee-ring region. The appearance of the TPhT was identified using its characteristic peak, according to previously reported studies. The peak at 649 cm^{-1} was identified as the vibrational mode of the C–Sn bond, the peaks at 617 cm^{-1}, 995 cm^{-1}, and 1019 cm^{-1} stand for the ring deformation vibration, the symmetrical breathing vibration, and δ(C–C–C) of the benzene ring. Together the presence of TPhT can be confirmed. Fig. 5a further proves the superiority in sensitivity of the inter-coffee-ring method by comparing the Raman intensity of TPhT at 10^{-2} M using the inter-coffee-ring on the light-confining structure, the single coffee-ring on the light-confining structure, and the single coffee-ring on the wafer. The light-confining structure significantly improved the

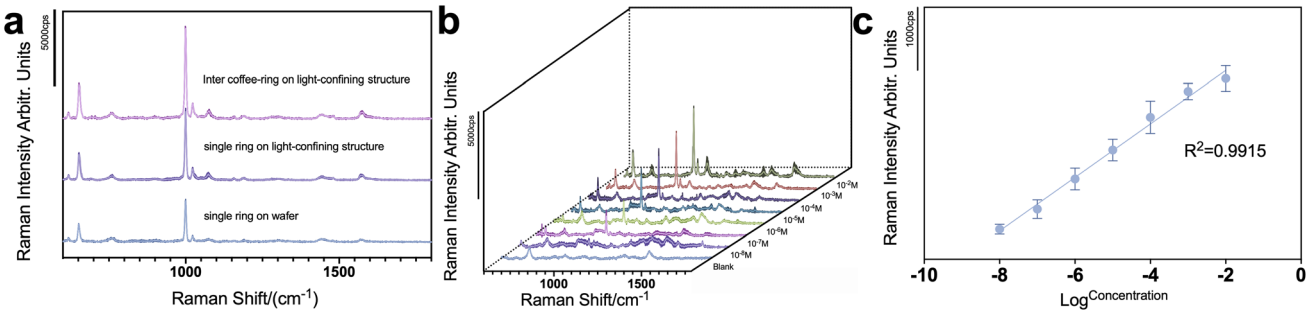

Fig. 5 (a) Raman spectra of 10^{-2} M TPhT using the inter-coffee-ring on the light-confining structure, a single coffee-ring on the light-confining structure, and a single coffee-ring on a wafer (laser power set to 7 mW), (b) SERS detection of TPhT spiked tap water with different concentrations, and (c) the linear regression of signal intensities at 995 cm^{-1} plot against log concentrations.

sensitivity of substrates and the intensity of inter-coffee-ring is obviously higher than that of single coffee-ring region. The limit of detection of TPhT on the substrate reached 10^{-8} M, as shown in Fig. 5b, and Fig. 5c presents the linear regression between Raman intensity and the concentration of the TPhT using 995 cm^{-1} as the reference peak. The linear coefficient R^2 of TPhT is 0.9915, which is highly reliable and feasible for the quantitative detection of TPhT. However, the use of water/methanol solute owing to poor solubility of TPhT in water lowers the contact angle of the sample on the light-confining structure, thus lowering the reproducibility of the substrates, especially when encountering other interference in the sample. Therefore, further improvements are needed in the inter-coffee-ring formation process to improve the feasibility of the sampling procedure and its reproducibility. Compared to previous studies,[27,28] our substrates reached a relatively high performance, the linearity is much better than 0.97 reported by Shan Jiang *et al.*, not to mention the semiquantitative detection reported by Juan Jiang *et al.* Although the sensitivity is relatively lower, it could easily be enhanced by altering the nanoparticle morphology. Most importantly, the rapid protocol enabled by the inter-ring method is significant for real sample detection.

Conclusions

A novel substrate based on the inter-coffee-ring effect is fabricated by coupling gold nanorods and a light-confining structure and demonstrates superiority in sensitivity, reproducibility, and stability. The coupling of gold nanorods and the light-confining structure enabled a 4.48-fold increase in signal intensity compared to gold nanorods distributed on wafers and a 294.07-fold increase compared to the light-confining structures. The R6G measurements proved its high sensitivity with a detection limit of 10^{-12} M. The coefficient of the variation of the spectra intensity is merely 3.12%, 37% of that acquired on a single coffee-ring mark, a testament to the substrates' high reproducibility. The barely changed inter-coffee-ring mark morphology after 30 min ultrasonication testified to its extremely high stability. In addition, the spiked TPhT detection reached the detection limit of 10^{-8} M with an R^2 of 0.9915, proving its feasibility in pollutant detection. The inter-coffee-ring effect enabled a rapid and low-cost protocol for pollutant detection, providing a reliable strategy for environmental monitoring.

Experimental

Materials

$HAuCl_4 \cdot 4H_2O$ (99.999%), CTAB (≥99.7%), $AgNO_3$ (≥99.8%), $NaBH_4$ (granular, 99.99% trace metals basis), and rhodamine 6G (99%) were purchased from Sigma-Aldrich Co., Ltd. Trisodium citrate (98%) and triphenylene chloride (96%) were supplied from Shanghai Macklin Biochemical Technology Co., Ltd. H_2SO_4 (95–98%), and EtOH (99.5%) were purchased from Chengdu Knowless Reagent Co., Ltd. *p*-ATP (≥97%), 1*H*, 1*H*, 2*H*, and 2*H*-perfluoro-decyl trichlorosilane (FDTS, 99%) were purchased from Beijing Solarbio Technology Co., Ltd. Deionized water was prepared by a molar water treatment system (Molecular® ΣH_2O System).

Instruments

The etching of the substrates was performed using Filmlab-R100 from Beijing Plasma Technology Co., China. The spin coater SPIN150i was from SPS electronic GmbH, Germany. The magnetron ion sputter was DP650 manufactured by ALLIANCE CONCEPT, France. Scanning electron microscopy was acquired using JSM-7800F made by JEOL, Japan. DSA100 completed the drop analysis from Kruss Scientific Instruments, Germany. Raman microscopy was acquired on Invia reflex from Renishaw plc., England.

Fabrication of the substrates

Light-confining structure fabrication. The light-confining structures were obtained by a standard photolithography process followed by wet etching. First, a thick layer of 200 nm chromium is magnetron sputtered on the silicon wafer as a mask layer. Then, the SU-8 photoresist is spin-coated on the above silicon wafer at a spin rate of 3000 rpm for 1 μm membrane thickness. Afterward, the SU-8 membrane was processed with soft baking, then exposed with a pattern generator to form a circled array pattern. The patterned wafer was then processed with post-baking. After that, it was soaked in the SU-8 developer to remove the excess photoresists, and a second post-

baking was processed to remove defects. The SU-8 membrane is now patterned as a circled array. After removing the extra chromium membrane, the substrates were soaked in wet etching reagents containing 30 wt% KOH at 80 °C and conducted wet etching with an etching rate of approximately 1 μm min^{-1}. After etching, the wafer is rinsed with deionized water, and the adhesive residue is removed with a dechromium solution. The final structure of the columnar tetragonal array is obtained.

Hydrophobic modification. The hydrophobic surface treatment is performed using FDTS as a modifier to chemically bond perfluorocarbon chains to the structure's surface through the high-temperature reaction of chlorosilanes and hydroxyl groups to reduce the surface energy of the substrate. Before surface modification, the silicon wafer surface was hydrophilically-modified by immersing in freshly prepared piranha solution for two hours to introduce hydroxyl groups providing binding sites for FDTS. The substrates were then immersed in a solution of FDTS in hexane at 0.1 wt% for 2 h, then rinsed three times with anhydrous ethanol and deionized water. At last, the substrates were annealed for 30 min at 80 °C to obtain superhydrophobicity.

Gold nanorod synthesis. Gold nanorods were prepared by the conventional seed growth method following a previously reported protocol.[29] The seed synthesis was performed in a 10 mL reaction system. First, a seed solution was prepared by mixing 100 μL 2.5 mM $HAuCl_4$ and 7.5 mL 0.1 M CTAB and diluted with deionized water to 9.4 mL. Then, 600 μL $NaBH_4$ at 10 mM was quickly added to the mixture under vigorous stirring for 2 min. The seed solutions are then placed in a water bath at 25 °C and allowed to grow for 2–6 hours. After seed growth, the growth of gold nanorods was carried out in a 100 mL reaction system. 1 mL of the seed solution was added to the growth solution containing 100 mL CTAB at 0.1 M, 1 mL $HauCl_4$ at 50 mM, 700 μL $AgNO_3$ at 0.01 M, 1 mL H_2SO_4 at 1 M, and 8 mL 0.1 M ascorbic acid. The addition sequence of the solutes is $HAuCl_4$, $AgNO_3$, and H_2SO_4; the solutions are orange in color after mixing. Then, the ascorbic acid is mixed with the solutions and rapidly changes to a colorless and transparent state. After full color transformation, the seed solution was rapidly injected into the mixture and allowed to vigorously stir for 2 min. Finally, the growth solution was left overnight at 30 °C. Then, the goldnanorods are washed with deionized water twice and redispersed in 5 mM CATB for further usage.

Rapid localizing and large area mapping

A localizing sample stage for the FESEM was manufactured to conduct *in situ* comparison of the inter-coffee-ring mark before and after ultrasonication. The sample stage consists of an aluminum plate with four alignment holes and a cover plate with four alignment pillars in the corner. The cover plate comprises an aluminum frame and a quartz plate with a coordinate ruler on its surface. The ruler on the surface is manufactured through the photolithography method. First, a 100 nm chromium film was magnetron sputtered on its surface, following spin coating of a photoresist film.

The photoresist was patterned with a pattern generator and a binary exposure machine. After which, the ruler pattern is formed with the chromium film exposed. After removing the exposed chromium film, the quartz plate conducted a reactive ion etching process under SF_6 and O_2 ambiance. A ruler featuring a recessed structure is now formed. Sequenced sputtering of 10 nm chromium film and 50 nm gold film is conducted in the structure to enhance the visibility, then the remaining photoresist and chromium film are removed. The specific sample stage morphology is illustrated in Fig. 2d.

Raman spectroscopy

All Raman spectra were acquired on the Renishaw Invia Reflex system. The 785 nm diode laser was selected for all tests to avoid fluorescent interference, and a 1200 L mm^{-1} grating was chosen according to the manufacturers' setup. The objective lens was set to 50× magnification, and each sample point was illuminated by laser for 10 s at different powers, with the accumulation time set to one. 35 mW laser power was used for R6G measurements, and the 3.5 mW laser power was fixed for TPhT detection. All spectra were acquired from 200 cm^{-1} to 2000 cm^{-1} in an extended mode, and the baseline was subtracted using a linear fit mode.

Numerical simulation

The electric field distribution of the substrates was acquired using COMSOL Multiphysics. A finite difference time domain (FDTD) method was applied in its simulation. The illuminating source was set to 785 nm using a plane wave. The mesh size was assigned to a range of 4×10^{-10} m to 5×10^{-9} m. The substrates were considered as nanopillars with a bottom radius of 400 nm, a top radium of 250 nm, and height of 1 μm. The result in this paper shows the y cross-section distribution of the electric field.

Author contributions

Dai Yujie performed the experiments and prepared the manuscript. Jiang Shuai and Gao Yangyang helped to revise the manuscript and conducted part of the experiments. Pan Hongyue and Liu Ke finished the sample stage manufacturing. Chang Lin conceived the idea, designed the experiment, and revised the manuscript.

Conflicts of interest

There are no conflicts to declare.

Acknowledgements

This work was financially supported by the Technical Innovation Project of Instrument and Equipment Function Development of the Chinese Academy of Sciences (field emission scanning electron microscope sample precision positioning analysis and linkage function development). Thanks to the Comprehensive Test Centre, Chongqing Institute of Green and

Intelligence Technology, Chinese Academy of Sciences, for technical support.

References

1 S. Jiang, L. Chang and J. Luo, Fabrication of a honeycomb-like bimetallic SERS substrate for the detection of triphenyltin chloride, *Analyst*, 2021, **146**, 6170–6177.
2 R. Pinto, R. Vilarinho and A. P. Carvalho, Raman spectroscopy applied to diatoms (microalgae, Bacillariophyta): prospective use in the environmental diagnosis of freshwater ecosystems, *Water Res.*, 2021, **198**, 117102.
3 R. Xu, R. L. Li and L. Y. Jia, An Efficient Strategy to Prepare Ultra-High Sensitivity SERS-Active Substrate Based on Laser-Induced Selective Metallization of Polymers, *ACS Sustainable Chem. Eng.*, 2021, **9**, 5038–5049.
4 L. Chang, S. Jiang and J. Luo, Nanowell-enhanced Raman spectroscopy enables the visualization and quantification of nanoplastics in the environment, *Environ. Sci.: Nano*, 2022, **9**, 542–553.
5 Q. Zhao, H. Yang and B. Nie, Wafer-Scale and Cost-Effective Manufacturing of Controllable Nanogap Arrays for Highly Sensitive SERS Sensing, *ACS Appl. Mater. Interfaces*, 2022, **14**, 3580–3590.
6 L. P. Xie, H. Zeng and J. X. Zhu, State of the art in flexible SERS sensors toward label-free and onsite detection: from design to applications, *Nano Res.*, 2022, **15**(5), 4374–4394.
7 S. He, W. Xie and S. Fang, Label-free identification of trace microcystin-LR with surface-enhanced Raman scattering spectra, *Talanta*, 2019, **195**, 401–406.
8 G. Pavliuk, D. Pavlov and E. Mitsai, Ultrasensitive SERS-Based Plasmonic Sensor with Analyte Enrichment System Produced by Direct Laser Writing, *Nanomaterials*, 2019, **10**, 14.
9 G. Xu, H. Cheng and R. Jones, Surface-Enhanced Raman Spectroscopy Facilitates the Detection of Microplastics <1 mum in the Environment, *Environ. Sci. Technol.*, 2020, **54**, 15594–15603.
10 X. H. Liu, H. Deng and L. Chang, Recent Progress of SERS for Environmental Estrogen Detection, *Spectrosc. Spectral Anal.*, 2020, **40**, 3038–3047.
11 D. Garcia-Lojo, S. Nunez-Sanchez and S. Gomez-Grana, Plasmonic Supercrystals, *Acc. Chem. Res.*, 2019, **52**, 1855–1864.
12 J. Langer, D. Jimenez de Aberasturi and J. Aizpurua, Present and Future of Surface-Enhanced Raman Scattering, *ACS Nano*, 2020, **14**, 28–117.
13 R. K. Gao, X. F. Song and C. B. Zhan, Light trapping induced flexible wrinkled nanocone SERS substrate for highly sensitive explosive detection, *Sens. Actuators, B*, 2020, **314**, 9.
14 X. Liu, J. Ma and P. Jiang, Large-Scale Flexible Surface-Enhanced Raman Scattering (SERS) Sensors with High Stability and Signal Homogeneity, *ACS Appl. Mater. Interfaces*, 2020, **12**, 45332–45341.
15 Y. Liu, M. Kim and S. H. Cho, Vertically aligned nanostructures for a reliable and ultrasensitive SERS-active platform: fabrication and engineering strategies, *Nano Today*, 2021, **37**, 26.
16 S. Kang, I. Kim and P. J. Vikesland, Discriminatory Detection of ssDNA by Surface-Enhanced Raman Spectroscopy (SERS) and Tree-Based Support Vector Machine (Tr-SVM), *Anal. Chem.*, 2021, **93**, 9319–9328.
17 H. J. Han, S. H. Cho and S. Han, Synergistic Integration of Chemo-Resistive and SERS Sensing for Label-Free Multiplex Gas Detection, *Adv. Mater.*, 2021, **33**, e2105199.
18 J. Bar, A. de Barros and D. H. S. de Camargo, Silicon Microchannel-Driven Raman Scattering Enhancement to Improve Gold Nanorod Functions as a SERS Substrate toward Single-Molecule Detection, *ACS Appl. Mater. Interfaces*, 2021, **13**, 36482–36491.
19 B. Han, Y. L. Zhang and L. Zhu, Direct laser scribing of AgNPs@RGO biochip as a reusable SERS sensor for DNA detection, *Sens. Actuators, B*, 2018, **270**, 500–507.
20 N. Chen, X. Meng and P. Ding, Biomimetic preparation of core-shell structured surface-enhanced Raman scattering substrate with antifouling ability, good stability, and reliable quantitative capability, *Electrophoresis*, 2019, **40**, 2172–2179.
21 S. Meng, R. Chen and J. Xie, Surface-enhanced Raman scattering holography chip for rapid, sensitive and multiplexed detection of human breast cancer-associated MicroRNAs in clinical samples, *Biosens. Bioelectron.*, 2021, **190**, 113470.
22 S. Pekdemir, I. Torun and M. Sakir, Chemical Funneling of Colloidal Gold Nanoparticles on Printed Arrays of End-Grafted Polymers for Plasmonic Applications, *ACS Nano*, 2020, **14**, 8276–8286.
23 A. Maimaiti, P. P. Patra and S. Jones, Low-Loss Hybrid High-Index Dielectric Particles on a Mirror for Extreme Light Confinement, *Adv. Opt. Mater.*, 2020, **8**, 1901820.
24 P. P. Gu, W. Zhang and Z. Y. Zhao, Engineering Colloidal Lithography and Nanoskiving to Fabricate Rows of Opposing Crescent Nanogaps, *Adv. Opt. Mater.*, 2020, **8**, 2000006.
25 S. E. J. Bell, G. Charron and E. Cortes, Towards Reliable and Quantitative Surface-Enhanced Raman Scattering (SERS): From Key Parameters to Good Analytical Practice, *Angew. Chem., Int. Ed. Engl.*, 2020, **59**, 5454–5462.
26 H. Alhmoud, D. Brodoceanu and R. Elnathan, A MACEing silicon: towards single-step etching of defined porous nanostructures for biomedicine, *Prog. Mater. Sci.*, 2021, **116**, 42.
27 S. Jiang, L. Chang and J. Luo, Fabrication of a honeycomb-like bimetallic SERS substrate for the detection of triphenyltin chloride, *Analyst*, 2021, **146**, 6170–6177.
28 J. Jiang, J.-M. Gao and J.-S. Guo, Identification and analysis of triphenyltin chloride with surface enhanced Raman scattering spectroscopy, *Chemosphere*, 2016, **161**, 96–103.
29 H. Y. Zhang, Y. W. Liu and M. F. S. Shahidan, Direct Assembly of Vertically Oriented, Gold Nanorod Arrays, *Adv. Funct. Mater.*, 2021, **31**(6), 2006753.